Chemistry Faculty Research & Creative Works   Chemistry

01 Jan 2023

Nanostructured Ternary Nickel-Based Mixed Anionic (Telluro)-Selenide as a Superior Catalyst for Oxygen Evolution Reaction

Ibrahim Munkaila Abdullahi

Siby Thomas

Alessio Gagliardi

Mohsen Asle Zaeem

et. al. For a complete list of authors, see https://scholarsmine.mst.edu/chem_facwork/3379

Recommended Citation

Nanostructured Ternary Nickel-Based Mixed Anionic (Telluro)-Selenide as a Superior Catalyst for Oxygen Evolution Reaction

Ibrahim Munkaila Abdullahi, Siby Thomas, Alessio Gagliardi, Mohsen Asle Zaeem, and Manashi Nath*

Developing protocols for designing high-efficiency, durable, cost-effective electrocatalysts for oxygen evolution reaction (OER) necessitates deeper understanding of structure–property correlation as a function of composition. Herein, it has been demonstrated that incorporating tellurium into binary nickel chalcogenide (NiSe) and creating a mixed anionic phase perturbs its electronic structure and significantly enhances the OER activity. A series of nanostructured nickel chalcogenides comprising a layer-by-layer morphology along with mixed anionic ternary phase are grown in situ on nickel foam with varying morphological textures using simple hydrothermal synthesis route. Comprehensive X-ray diffraction, X-ray photoelectron spectroscopy, and in situ Raman spectroscopy analysis confirms the formation of a trigonal single-phase nanocrystalline nickel (telluro)-selenide (NiSeTe) as a truly mixed anionic composition. The NiSeTe electrocatalyst exhibits excellent OER performance, with a low overpotential of 300 mV at 50 mA cm^{-2} and a small Tafel slope of 98 mV dec^{-1} in 1 M KOH electrolyte. The turnover frequency and mass activity are 0.047 s^{-1} and 90.3 A g^{-1}, respectively. Detailed electrochemical measurements also reveal enhanced charge transfer properties of the NiSeTe phase compared to the mixture of binaries. Density functional theory calculations reveal favorable OH adsorption energy in the mixed anionic phase compared to the binary chalcogenides confirming superior electrocatalytic property.

1. Introduction

Electrochemical water splitting is among the most significant and attractive clean hydrogen generation technology. Hydrogen is

I. M. Abdullahi, M. Nath
Department of Chemistry
Missouri University of Science and Technology
Rolla MO 65409, USA
E-mail: nathm@mst.edu

S. Thomas, A. Gagliardi
School of Computation, Information, and Technology
Technical University of Munich (TUM)
85748 Garching, Munich, Germany

M. A. Zaeem
Department of Mechanical Engineering
Colorado School of Mines
Golden, CO 80401, USA

ⓘ The ORCID identification number(s) for the author(s) of this article can be found under https://doi.org/10.1002/ente.202300177.

considered to be an ideal renewable energy source to substitute conventional fossil fuels owing to its zero-carbon emission, intense energy density, and the ability to utilize periodic renewable energy such as wind and solar energy.[1] However, due to the high energy requirement for water oxidation reaction, practical water electrolyzers operate at a much higher voltage (1.8–2.0 V) relative to the theoretical water splitting voltage of 1.23 V, leading to a large overpotential.[2] The use of efficient electrocatalysts in anodic oxygen evolution reaction (OER) and cathodic hydrogen evolution reaction (HER) can effectively decrease the overpotential and improve the sluggish kinetics of HER/OER and therefore enhance the energy efficiency of the process.[3]

To date, the state-of-the-art electrocatalysts for HER are mostly Pt-based materials,[4,5] whereas the oxides of precious metals such as Ru or Ir are used as electrocatalysts for OER.[6] These precious metals, however, are scarce and expensive, limiting their widespread usage. Over the last several decades, it has become apparent that implementing large-scale water electrolysis will require the development of high-efficiency electrocatalysts, preferably composed of earth-abundant nonprecious elements. Extensive research into designing such new electrocatalysts from earth-abundant elements has led to a class of catalyst compositions that exceed the present capabilities. Apart from enhanced performance, these novel compositions also broaden the knowledge and understanding of the factors that determine catalytic activity in order to customize catalyst surfaces atom by atom.[7]

The electrocatalytic properties of any material are primarily influenced by its electronic structure, which depends on the central metal atom as well as the coordinating ligands. Hence, the main goal is to design catalysts through a proper understanding of structure–property correlation by varying the composition and physical structure of materials and understanding its effect on catalytic efficiency. Considerable attempts have been made to design efficient electrocatalysts for OER and HER comprising earth-abundant elements. Appreciable progress has been made over the last few years in designing highly active OER catalysts based on metal phosphate,[8–10] oxides,[11] chalcogenides,[12–14]

hydroxides,[15] and metal complexes.[16,17] Some of these phosphates, chalcogenides, and some carbides have been used as HER catalysts.[18–21] Among these transition metal chalcogenides, particularly metal sulfides, selenides, and tellurides, have made a significant impact as electrocatalysts in water oxidation due to their unprecedented high catalytic activity,[12,22–24] which is exemplified by their extremely low overpotential and high current density. One of the most commonly used commercial OER/HER electrocatalysts is porous Ni, due to its low cost, high robustness, and moderate catalytic activities. Also, it has been observed that in Ni-based chalcogenides, reducing anion electronegativity from O to Te (electronegativity order: E = Te (2.1) < Se (2.55) < S (2.58) < O (3.44)) leads to significant improvement in the intrinsic catalytic properties.[12,24,25] This was primarily attributed to increased covalency in the Ni–chalcogen (Ni–E) bond with reduced anion electronegativity down the chalcogens group, i.e., covalency order Ni–O < Ni–S < Ni–Se < Ni–Te. Such an increase in covalency leads to the adjustment of the electronic band structure and better alignment of the valence and conduction band edges with the water oxidation/reduction level. Better band alignment enhances facile charge transfer at the electrolyte–electrocatalyst interface which subsequently minimizes the overpotential for water oxidation/reduction. A critical factor in catalyst design is the ability to understand and predict the catalytic activity through systematic variation of composition. The chalcogenide series presents an ideal opportunity to understand the effect of anion electronegativity and lattice covalency on the electrocatalytic properties through anion substitution. Mixed anionic systems will be especially interesting for understanding the subtle effect of tunable anion electronegativity. One of the probes for understanding the direct effect of anion electronegativity on the catalytic activity is the hydroxyl (–OH) adsorption energy on the catalyst site, which is considered as the primary surface activation step. Hence, investigation of the –OH adsorption energy will be a key component for developing effective catalyst design principles. The mixed anionic chalcogenides offer a unique opportunity for investigating the subtle effects of changing electronegativity on the –OH adsorption energy because these systems offer more systematic control of electronic band structure and electrochemical tunability.[26,27] To the best of our knowledge, such mixed anionic chalcogenides have not been reported for electrocatalytic water-splitting reactions.

We report herein a novel nanocrystalline nickel (telluro)selenide (NiSeTe) material grown on Ni foam (NF) by one-pot in situ hydrothermal method as an efficient water oxidation catalyst. We also illustrate the effect of adjusting the electronic structure of nickel-selenide (NiSe) by Te incorporation to form the mixed anionic coordination where both Se and Te are coordinated to the same catalytic (Ni) site. NiSeTe catalyst combines the characteristic favorable reaction kinetics and the synergistic effects between NiSe and nickel-telluride (NiTe) catalysts, as well as the stability of the nickel-supported structure. These mixed anionic compositions exhibit a significantly lower OER overpotential of 300 mV at 50 mA cm^{-2} and a small Tafel slope (98 mV dec^{-1}). Density functional theory (DFT) calculations show favorable OH adsorption energy as well as the charge transfer between the OH$^-$ ion and the surface of NiSe, NiTe, and NiSeTe compositions during OER. The enhanced conductivity of NiSeTe can encourage fast electron transfer between the active

NiSeTe composition while the nanostructured surface provides abundant surface area and active sites. This NiSeTe electrode based on nonprecious Ni metal exhibits superior catalytic performance and durability toward water oxidation in strongly alkaline media. This study is of a more fundamental nature exploring the effect of mixed anionic coordination on the electrochemical activity and comparing that with the mixture of binary phases. The results reveal that a subtle change in the nearest neighbor coordination to the catalytically active site leads to significant changes in the electrocatalytic activity. These results unlock exciting new avenues to explore mixed-chalcogenide electrocatalysts for water splitting and to understand structure−property−activity relationships for advanced catalysts with industrial scalability.

2. Results and Discussion

Details of the hydrothermal synthesis along with a description of the layer-by-layer in situ deposition scheme are provided in the supporting information. The general synthesis and composition of each catalyst as grown on NF are schematically illustrated, as presented in **Figure 1**. Throughout this article, NiSe@NiTe represents NiSe grown on top of NiTe which was first grown on NF substrate. And, NiTe@NiSe describes NiTe grown on top of NiSe which was first grown on NF substrate. Both NiSe@NiTe and NiTe@NiSe represent a layer-by-layer morphology. The NiSeTe composition, on the other hand, represents the true mixed anionic phase of NiSeTe grown on an NF substrate. All the samples show a rough surface morphology relative to pure NF substrate indicating successful sample deposition on the NF substrate.

Scanning electron microscopy (SEM) images (**Figure 2**a–f and Figure S1, Supporting Information) showed clear evidence of distinct phase growth of different morphologies as indicated by homogeneously covered densely packed nanostructured particles grown on NF. The morphologies exhibit some degree of surface roughness. NiTe and NiTe@NiSe show a clustered nanosheet-like structure, and NiSeTe, NiSe, and NiSe@NiTe exhibited homogeneous growth of vertically interconnected grains. The porous nature of NF catalyst systems is believed to enhance accessibility to catalytic sites. Surface elemental compositions of NiSeTe, NiSe@NiTe, and NiTe@NiSe were estimated from energy-dispersive X-ray spectroscopy mapping analysis (Figure S2, Supporting Information). It shows the average surface atomic ratio of Ni:Se (1:1) in NiSe@NiTe, suggesting NiSe dominated surface and NiTe bottom layer. Similarly, NiTe@NiSe showed the average surface atomic ratio of Ni:Te (1:1), implying the NiTe surface layer and NiSe bottom layer. NiSeTe revealed Se:Te (1:1) surface atomic ratio, confirming NiSeTe composition. The cross-sectional SEM analysis showed the different phases in the nickel chalcogenide composite samples (Figure 2g–i). NiSe@NiTe showed two phases supported by NF substrate: NiSe phase surface layer and NiTe phase bottom layer (Figure 2g). Similarly, NiTe@NiSe displayed two phases: NiTe phase surface layer and NiSe phase bottom layer, as shown by elemental mapping analysis in Figure 2i. This is consistent with the layer-by-layer hydrothermal growth hypothesis, suggesting that NiTe@NiSe and NiSe@NiTe each comprise two distinct layered phases rather than random phase distribution. Conversely, NiSeTe shows a single phase, corresponding to
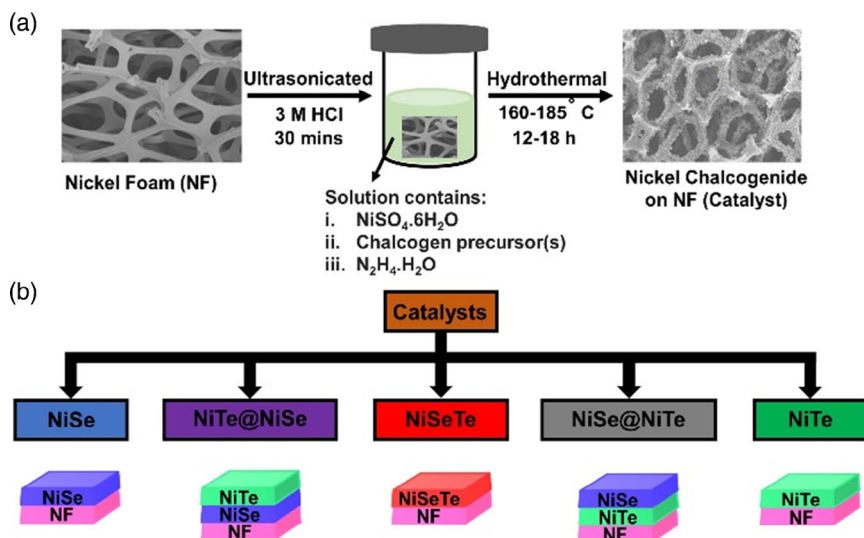
ADVANCED
SCIENCE NEWS
www.advancedsciencenews.com

Energy Technology
Generation, Conversion, Storage, Distribution
www.entechnol.de

Figure 1. Schematic describing the a) preparation of nickel mixed anionic chalcogenide; b) composition of catalyst deposited on NF.
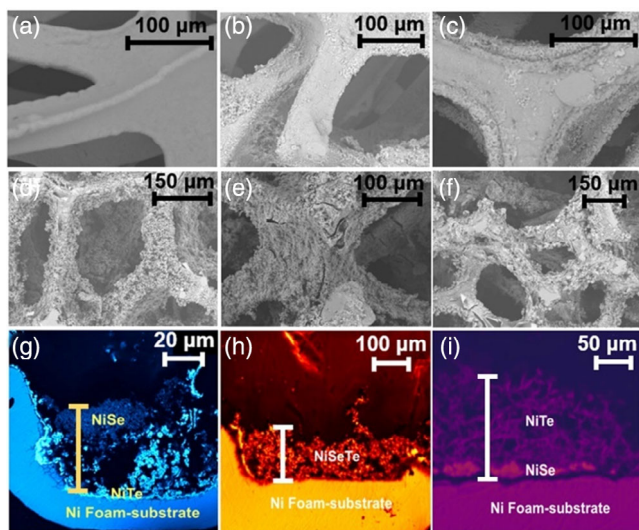

Figure 2. SEM images of a) NF; b) NiSeTe; c) NiSe; d) NiTe@NiSe; e) NiSe@NiTe; f) NiTe; cross-sectional SEM-EDX images of g) NiSe@NiTe with a thickness of 45 μm; h) NiSeTe with a thickness of 135 μm; and i) NiTe@NiSe with a thickness of 124 μm.

the NiSeTe phase. The cross-sectional SEM images were also used to estimate the thickness of the individual layers. NiSe@NiTe showed a composite layer thickness of 45 μm with the NiSe layer being approximately 20 μm thick atop a 25 μm NiTe layer. Similarly, the NiTe@NiSe deposition showed a composite layer thickness of ≈124 μm with a 20 μm NiSe layer below an approximately 100 μm NiTe layer. The NiSeTe, on the other hand, showed a deposition thickness of 134 μm. These results are consistent with the cross-sectional EDX analysis data obtained for these samples (Figure S3–S5, Supporting Information).

The NiTe@NiSe and NiSe@NiTe composites both yielded NiSe and NiTe mixed phases, as observed in the powder X-ray diffraction (PXRD) patterns shown in **Figure 3**a,b, rather than a new

resultant phase. The NiTe@NiSe composite (Figure 3d) shows peaks at 124 and 143 cm^{-1} in Raman, corresponding to A_g and T_g modes in NiTe, indicating the dominance of NiTe on the surface. Conversely, the NiSe@NiTe composite (Figure 3e) shows Raman peaks at 262, 226, 181, and 141 cm^{-1} corresponding to T_g, A_g, E_g, and T_g in NiSe, respectively,[28,29] implying NiSe dominated the surface (see Figure S6, Supporting Information). This is consistent with the layer-by-layer deposition growth order of the composites. Binary NiSe and NiTe are used as a reference in this study, characterized as shown in Figure S6, Supporting Information. The XRD patterns for NiTe and NiSe were identical to the standard diffraction patterns (PDF # 01-075-0610) and (PDF # 01-089-2019), respectively. Their surface Raman spectra show peaks at 147, 225, and 265 cm^{-1} which corresponds to T_g, A_g, and T_g modes in NiSe (Figure S6, Supporting Information), and peaks at 125 and 143 cm^{-1} presenting to A_g and T_g in NiTe (Figure S6, Supporting Information), both of which were consistent with the reported literature.[29,30] The crystal structure of NiSe (Figure S7, Supporting Information) changes after hydrothermal tellurization into a single-phase trigonal NiSeTe nanocrystalline material as shown in the PXRD pattern in Figure 3c. NiSeTe occurs as a "Kitkaite" mineral and exhibits CdI$_2$-like trigonal crystal structure with $P\bar{3}m1$ space group of $\bar{3}m$ crystal class (Figure S7, Supporting Information), similar to previous reports.[31] The PXRD peaks at 31.51, 43.41, 47.22, 49.95, and 59.5°, were indexed to (011), (012), (110), (111), and (201) planes of trigonal NiSeTe, respectively (Figure 3c), which is consistent with its standard diffraction pattern (PDF # 01-089-2022). Both Se and Te in NiSeTe have a site occupancy factors (SOF) of 0.5 for equivalent crystallographic positions; consequently, Ni(1)–Se(1)/Ni(1)–Te(1) bond lengths are all equivalent (2.499 Å).

In this structure, the cations are no longer connected in the *c* direction and neighboring layers are held together by van der Waals forces only.

NiSeTe possesses metallic-like properties; hence, it has been reported to show weak and temperature-independent
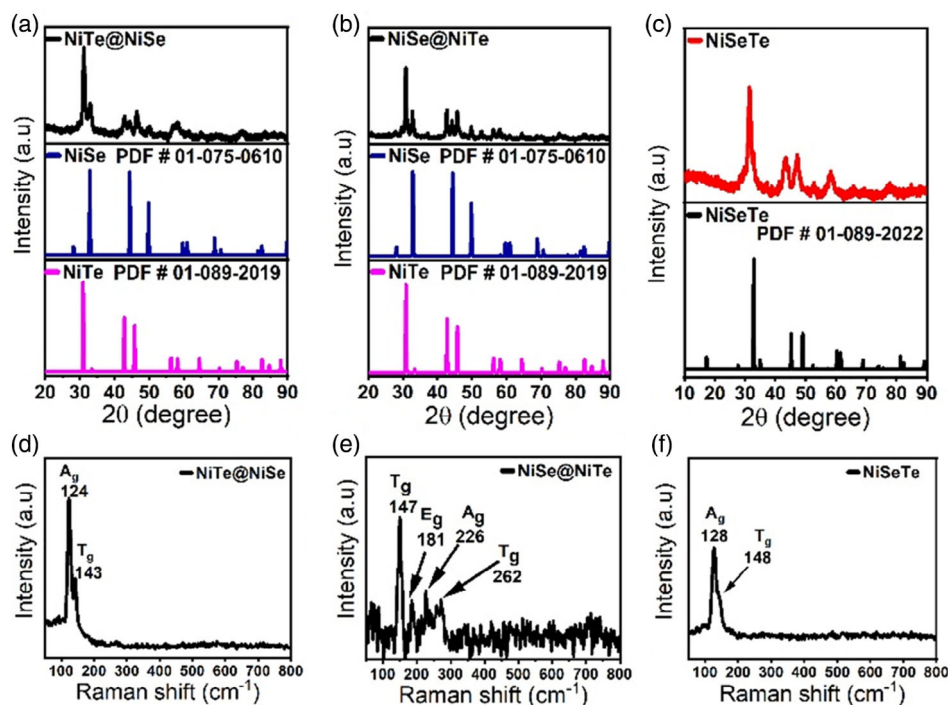
Figure 3. XRD spectra of a) NiTe@NiSe; b) NiSe@NiTe; c) NiSeTe; Raman spectra of d) NiTe@NiSe; e) NiSe@NiTe; and f) NiSeTe.

paramagnetism.[31] The calculated unit cell parameters from the Rietveld refinements are $a = b = 3.716(5)$ Å and $c = 5.126(5)$ Å for trigonal NiSeTe. Furthermore, Raman at 128 and a shoulder at 148 cm^{-1} correspond to A_g and T_g modes in NiSeTe (Figure 3f). This is consistent with averaging the Ni–Te and Ni–Se modes, as reported in similar composition types,[29] supporting the coordination of both chalcogens (Se and Te) to the same metal atom (Ni) resulting in a true mixed anionic composition. The average crystallite size of NiSeTe was estimated to be 7.1 nm. This was calculated from the Scherrer equation (See Equation in S4, Supporting Information) by fitting (011), (012), and (110) XRD reflection peak(s) using Lorentz function.[32,33]

X-ray photoelectron spectroscopy (XPS) spectra of the as-prepared NiSe@NiTe show Ni 2p at 873.7 and 855.8 eV assigned to the Ni^{2+} oxidation state in mostly the surface layer (NiSe) of the NiSe@NiTe, with satellite peaks at positions 880.28 and 861.6 eV corresponding to Ni 2$p_{3/2}$ and Ni 2$p_{1/2}$, likely coming from NiSe and NiTe mixed phases. The higher binding energy of Ni 2p in NiSe@NiTe than that of NiTe indicates the strong synergetic interactions between the two layers; a similar observation has been reported previously.[34] The Se 3d and Te 3d spectra are shown as insets of Figure S8, Supporting Information. The Se 3d spectrum indicates three peaks after deconvolution at 58.6, 57.6, and 54.8 eV corresponding to SeO$_x$, Se 3$d_{3/2}$, and Se 3$d_{5/2}$ respectively, indicating surface selenium oxidation. Interestingly, the inset showing Te 3d spectrum indicated very faint low-intensity peaks at 576.3 and 586.9 eV corresponding to Te 3$d_{5/2}$ and Te 3$d_{3/2}$, respectively. This indicates that the surface of NiSe@NiTe is mostly NiSe and has very little NiTe on it, which is consistent with layer-by-layer compositional growth.

The binding energy of the Se 2p peak in NiSe@NiTe is lower than that of NiSe, suggesting extra charges in the Se, indicating electronic interactions. This phenomenon indicates that interfacial charge transfer may occur to Se from other atoms.[34,35] The interfacial electronic interactions between NiTe and NiSe provide promising opportunities for modulating electrocatalytic properties. While the XPS spectra of NiTe@NiSe show Ni 2p at 873.7 and 855.8 eV assigned to the Ni^{2+} oxidation state of NiTe in NiTe@NiSe. The satellite peaks at positions 880.28 and 861.6 eV correspond to Ni 2$p_{3/2}$ and Ni 2$p_{1/2}$. The two insets correspond to Se 3d and Te 3d spectra, respectively (Figure S9, Supporting Information). The Se 3d spectrum shows no Se 3$d_{5/2}$ and Se 3$d_{3/2}$ and/or SeO$_x$ peaks, indicating that the NiTe surface coverage is more effective than when NiSe is serving as the top surface layer. Again, this is consistent with layered growth. Further, the inset showing Te 3d spectrum displays peaks at 576.3 and 586.9 eV assigned to Te 3$d_{5/2}$ and Te 3$d_{3/2}$, respectively, suggesting the surface is mainly NiTe (inset of Figure S9, Supporting Information).

High-resolution XPS of NiSeTe shows Ni 2p peaks at 874.5 and 856.6 eV (**Figure 4**a) assigned to the Ni^{2+} oxidation state, while peaks at 880.6 and 862.4 eV are due to Ni 2$p_{3/2}$ and Ni 2$p_{1/2}$ satellite peaks. The peak at 853.1 eV representing Ni^0 corresponds to metallic Ni 2p arising from the NF substrate or from excess unreacted Ni^0 from reduced Ni^{2+} precursor. XPS spectra of Te and Se are shown in Figure 4b,c, respectively. The Se 3d deconvoluted spectrum shows three peaks at 59.0, 57.4, and 54.7 eV corresponding to SeO$_x$, Se 3$d_{3/2}$, and Se 3$d_{5/2}$ respectively. The binding energy of the Se 2p peak is slightly lower than that of NiSe, suggesting extra charges in the Se due to electronic interactions. This phenomenon indicates possible interfacial
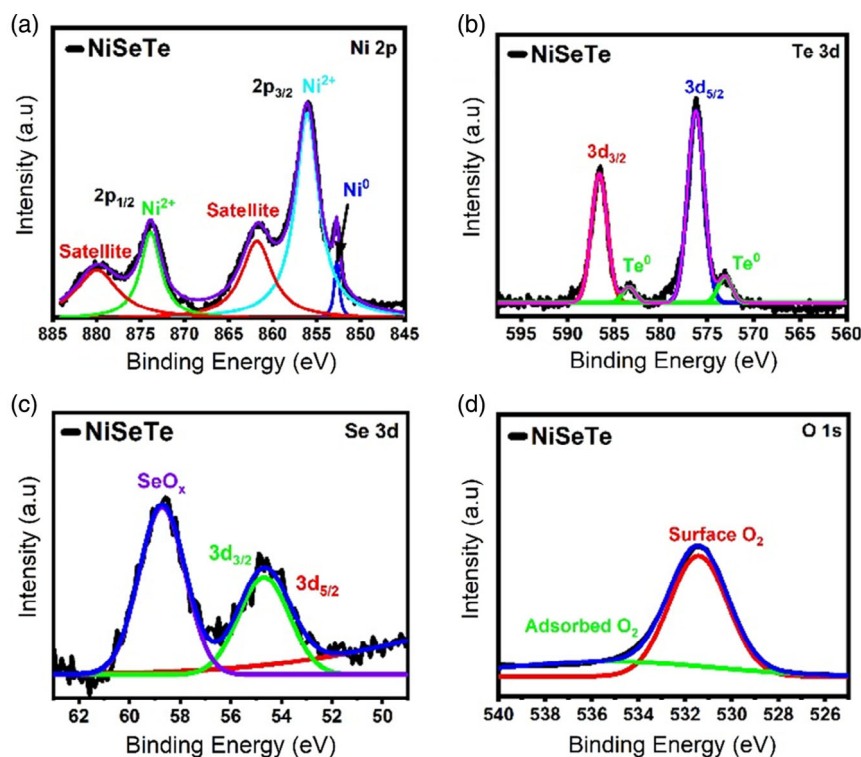
Figure 4. The high-resolution XPS spectra of NiSeTe a) Ni $2p$ peak; b) Te $3d$ peak; c) Se $3d$ peak; and d) surface O $1s$ peak.

charge transfer from Te and Ni to Se.[34,35] The oxidation states of Se were recognized as Se^{2-} and Se^{4+}, corresponding to NiTeSe and SeO_2. SeO_2 could either be from mild surface oxidation of the Se in the system or from excess unreacted SeO_2 adsorbed on the surface.

The C $1s$ and O $1s$ signals are largely due to the surface adsorption of atmospheric adventitious carbon and oxygen species. Furthermore, the Te $3d$ spectrum shown in (Figure 4b) indicated peaks at 576.4 and 586.9 eV which were ascribed to Te $3d_{5/2}$ and Te $3d_{3/2}$, respectively. The Te spectrum also indicated the presence of metallic Te at 573.0 and 583.4 eV. This could be coming from surface-adsorbed traces of unreacted Te generated from the reduction of the TeO_2 precursor in the reaction mixture. This type of observation is well documented in the literature.[20,24] The peak positions of the binding energies in the mixed anionic ternary NiSeTe phase are slightly shifted to more positive values relative NiSe phase due to differences in the coordination and difference in electronic structure which leads to subtle variation in electron density distribution, in agreement with previous reports.[12,36,37] The binding energies for Ni $2p$, Se $3d$, and Te $3d$ in the XPS study of NiSe and NiTe (Figure S10, Supporting Information) are also in agreement with the reported literature.[14,34,38]

Nickel chalcogenides have shown superior electrochemical performance for OER and overall water splitting.[39,40] Both NiTe[34] and NiSe[38] grown on NF as nanoarray and nanowire film, respectively, have shown excellent OER and HER performance. In addition, a vertically grown catalyst on NF with a porous structure type is highly beneficial for OER, as it provides easier accessibility to active catalytic surface area for reactive substrates,[41] which plays

a vital role in electrolyte diffusion and gas discharge. In this work, OER electrocatalytic performance NiSe@NiTe and NiTe@NiSe catalysts were compared to NiSeTe in O_2-saturated 1 M KOH measured under the same conditions, to elucidate the effect of mixed anionic coordination. The polarization curves from iR-corrected linear sweep voltammetry (LSV) scans (**Figure 5**a) indicate their OER performance, during which oxygen bubbles are observed from the electrode surface. The oxidation peaks around 1.37 V (versus RHE) correspond to the Ni^{2+} to Ni^{3+} redox couple, which shifts slightly on changing the anion composition.[25] This observation was consistent with the shift noticed in the comparative cyclic voltammetry measurements conducted for these nickel series samples (Figure S11, Supporting Information). In this series of compounds, NiTe exhibits the best activity toward OER, exhibiting an overpotential of 260 mV to achieve the current density of 50 mA cm^{-2}. The NiSe does not show any obvious anodic current until the potential reaches $\approx$1.53 V. In contrast, the NiSeTe-modified electrode displayed the onset of OER much earlier and achieved significantly higher catalytic current, thereby demonstrating excellent activity with a low overpotential requirement of 300 mV to reach 50 mA cm^{-2}. The comparative efficiency toward OER for the nickel chalcogenides series is in the order NiTe > NiSeTe > NiSe, illustrating the critical effect of decreasing anion electronegativity around the catalytically active Ni center. As anion electronegativity decreases, covalency increases, thereby affecting the electronic structure and increasing the valence band edge comparable to the OER energy level.[26] The OER performance of layer-by-layer binary phases, NiSe@NiTe, and NiTe@NiSe at 100 mA cm^{-2} relative to the single-phase

ADVANCED
SCIENCE NEWS
www.advancedsciencenews.com

Energy Technology
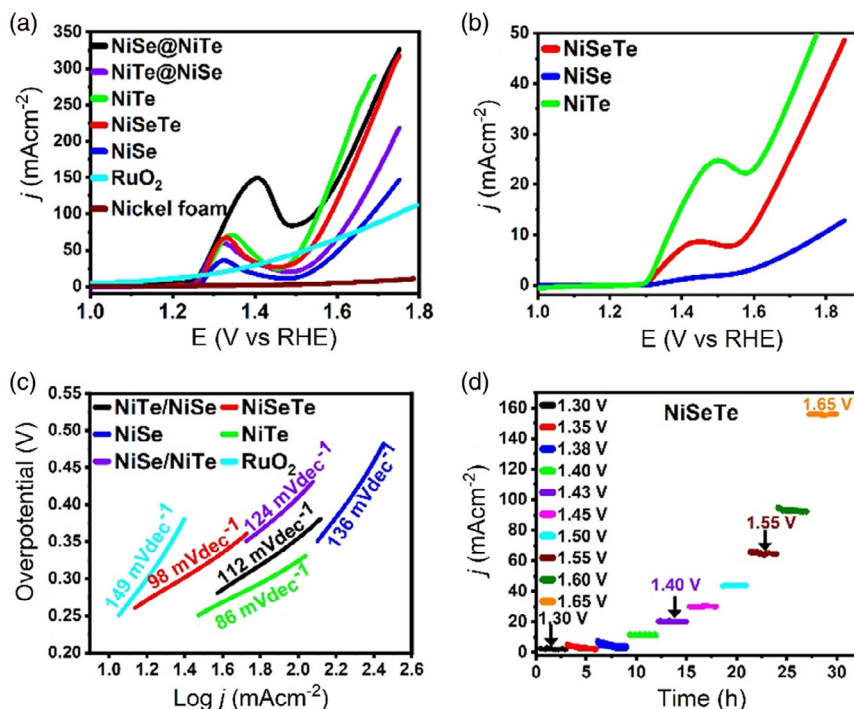Generation, Conversion, Storage, Distribution
www.entechnol.de

Figure 5. a) LSV plots of catalysts on NF; NiSe@NiTe (black), NiTe@NiSe (violet), NiSeTe (red), NiSe (blue), NiTe (green) RuO₂ (cyan), and NF (brown); b) LSV of catalysts on carbon cloth; NiSeTe (red), NiSe (blue), NiTe (green); c) the Tafel slope obtained from LSV plots for different catalysts; and d) multistep chronoamperometry study of the NiSeTe on NF electrode carried out at various constant applied potentials.

mixed anionic compositions is in the order NiTe > NiSe@NiTe > NiSeTe > NiTe@NiSe > NiSe (**Table 1**). Powder samples of NiTe, NiSeTe, and NiSe drop-casted on carbon-cloth substrate exhibited identical electrocatalytic activity trends as those samples grown hydrothermally on NF (NiTe > NiSeTe > NiSe) (Figure 5b).

This confirms the inherent properties of these catalysts. However, a much higher current density is generated with a directly grown catalyst on a highly conducting substrate which is particularly beneficial in practical water electrolysis.

Tafel plots shown in Figure 5c reveal reaction kinetics in the electrocatalytic OER with a lower Tafel slope indicating faster kinetics. The Tafel slope showed an increase in the order NiTe ($86\,mV\,dec^{-1}$) < NiSeTe ($98\,mV\,dec^{-1}$) < NiSe@NiTe ($112\,mV\,dec^{-1}$) < NiTe@NiSe ($124\,mV\,dec^{-1}$)

< NiSe ($136\,mV\,dec^{-1}$), indicating that NiTe has the fastest OER kinetics, in agreement with the observation of electrocatalytic activity. Conversely, the NiSe catalyst shows the highest Tafel slope value, corresponding to the slowest OER kinetics in the nickel chalcogenide series. Interestingly, NiSeTe exhibited a Tafel slope value, intermediate between the NiTe and NiSe. This suggests that changing the chalcogen anion from a more electronegative Se to a less electronegative Te facilitates the OER kinetics. Multistep chronoamperometry test on NiSeTe at different applied potentials between 1.30 and 1.65 V versus RHE shows no obvious degradation of current density under any of the tested applied potentials (Figure 5d). This demonstrates the superior reliability of NiSeTe catalyst within a wide potential range, as well as its high mass transport, and mechanical robustness toward longevity in OER activity.

Table 1. Electrocatalytic parameters compared in nickel series catalytic systems.

Material	NiTe	NiSe	NiSeTe	NiTe@NiSe	NiSe@NiTe
Onset potential/V	1.43	1.53	1.48	1.51	1.47
Overpotential @ 50 mA cm^{-2} [mV]	260	380	300	350	–
Overpotential @ 100 mA cm^{-2} [mV]	320	450	350	400	310
Ni^{2+} → Ni^{3+} oxidation peak potential [V]	1.36	1.32	1.34	1.33	1.42
Current density @ 300 mV [mA cm^{-2}]	70.09	19.46	56.64	36.04	97.39
Tafel slope [mV dec^{-1}]	86	136	98	124	112
Mass activity [Ag^{-1}]	138.1	33.7	90.3	29.2	57.1
TOF [s^{-1}]	0.065	0.009	0.047	0.025	0.048

The $Ni^{2+} \rightarrow Ni^{3+}$ preoxidation peak typically observed in OER of Ni-based systems provides an insight into the inherent property of the catalyst concerning its activation step.[42,43] Additionally, the position of the Ni^{2+}/Ni^{3+} oxidation peak is generally affected by the electronegativity of anion and coordination type around the Ni central atom.[24] This effect is observed in the $Ni^{2+} \rightarrow Ni^{3+}$ oxidation peak potential (Table 1). It must be noted here that the effect of the thickness of grown catalyst layers was not moderated, although the sample loading was roughly comparable (Equation S5 and S6, Supporting Information). For highly moderated samples, oxidation peak potential can be used to distinguish surface compositions. As changes in anion composition and film thickness in catalysts could shift the Ni^{2+} oxidation peak position, one should be extremely quantitative when using this approach as a tool to appreciate the compositional evolution of active surfaces adequately.

The electrocatalytic performance toward OER can be substantially influenced by electronic structure, which is a direct consequence of the chemical composition as well as the crystal lattice structure of the electrocatalyst.[7,37] Selenides have higher electronegativity and harder base characteristics, with a lesser degree of electron cloud delocalization, hence lower conductivity and charge mobility compared to telluride.[20] Consequently, nickel selenides show lower electrocatalytic activity toward OER. However, changing covalency around the catalytically active Ni site leads to rearrangement of the electronic band structure and movement of the valence and conduction band edges closer to the water oxidation-reduction level, consequently reducing the overpotential requirement. It is therefore recommended that bond energies of intermediates and electronic structure (through chemical composition and crystal structure) should be tuned in

catalysts to enhance OER performance.[7,40] In NiSeTe crystal structure (trigonal), Ni atoms have unique coordination environments than those of NiSe and NiTe (hexagonal), thereby influencing its electrocatalytic activity toward OER.

To further appreciate the excellent OER performance of these nickel chalcogenide systems, the Tafel plot, mass activity, turnover frequency (TOF), and electrochemical impedance spectroscopy (EIS) were computed as summarized in **Figure 6**. NiTe and NiSeTe catalysts exhibited the highest specific mass activities of 138.1 and 90.3 Ag^{-1}, respectively, at 0.36 V overpotential (Figure 6b). TOF achieved for NiSeTe is 0.047 s^{-1} at the overpotential of 0.36 V, which was threefold (3X) higher than NiSe. NiTe attained the highest TOF of 0.065 s^{-1} (Figure 6c). This demonstrates the higher intrinsic activity of NiSeTe and NiTe implying higher active sites and larger electrochemical surface area. The EIS analysis verified the fast OER kinetics of the catalysts. The charge-transfer resistance on NiSeTe at 1.55 V is 3.10 Ω, slightly smaller than that of NiSe@NiTe (3.55 Ω) and NiTe@NiSe (4.31 Ω) (Table S1, Supporting Information), under similar conditions, implying faster electron transport in the NiSeTe. This is consistent with high activity kinetics observed in the nickel series. Overall, the charge transfer resistance follows the trend, NiTe (1.37 Ω) > NiSeTe (3.10 Ω) > NiSe@NiTe (3.55 Ω) > NiTe@NiSe (4.31 Ω) > NiSe (5.05 Ω), which corroborates well with the observed high catalytic efficiency.[22] The electrolyte resistance of NiSeTe is 26.0 Ω, substantially smaller than that of NiSe@NiTe (53.0 Ω), NiSe (42.32 Ω), NiTe (39.08 Ω), and NiTe@NiSe (37.99 Ω). The substrate–catalyst surface coverage resistance observed in some of the catalysts showed the least value in NiSeTe (29.00 Ω). The double layer capacitance on NiTe (350 μF), NiSe (43 μF), and NiTe@NiSe (279 μF) is smaller
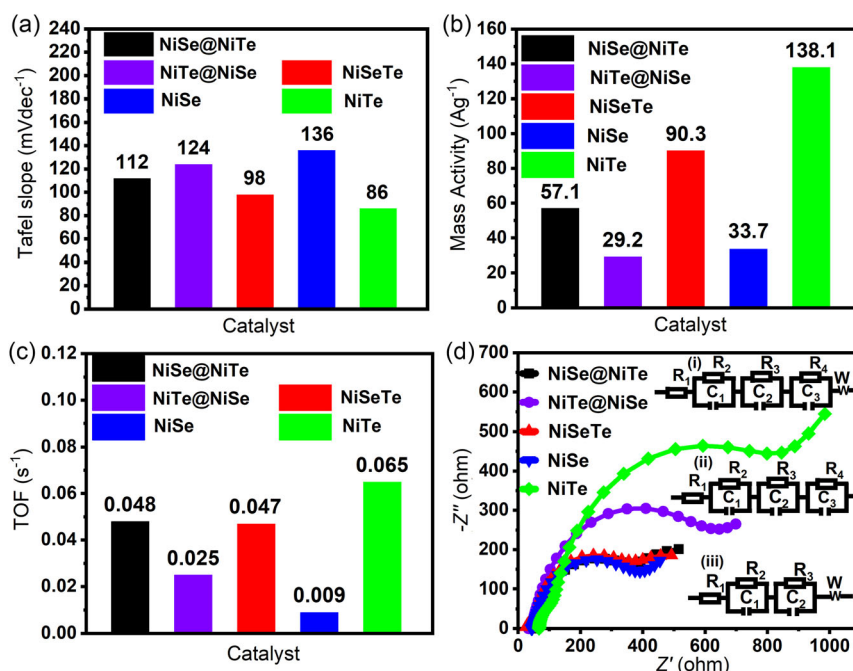

Figure 6. Electrocatalytic performance of NiSe@NiTe (black), NiTe@NiSe (violet), NiSeTe (red), NiSe (blue), and NiTe (green) catalysts: a) Tafel slopes; b) mass activity at $\eta = 0.36$ V; c) TOF at $\eta = 0.36$ V; and d) Nyquist plots in the AC frequency range between 100 kHz and 0.1 Hz, at 1.55 V versus RHE. The inset in (d) shows the fitted equivalent circuit for i) NiTe; ii) NiSeTe and NiSe@NiTe; and iii) NiSe and NiTe@NiSe.

ADVANCED
SCIENCE NEWS
www.advancedsciencenews.com

Energy Technology
Generation, Conversion, Storage, Distribution
www.entechnol.de

than that of NiSeTe (38.0 mF). The above observation implied that the diffusion effect on (NiTe, NiTe@NiSe, and NiSe) is more significant, as confirmed by their Warburg diffusion element contributions.[44] Enhancement in electrocatalytic performance has been previously reported, ascribed to the synergistic effect of combining multicomponent compositions,[45,46] and heteroatomic doping, which could either be cationic, anionic, as well as interfacial engineering from the effects of ligands and electronic interactions around the different active centers.[47] Incorporation of Te into NiSe results in electron density redistribution around the catalytically active Ni species in the resulting NiSeTe. This enables enhanced charge transport on surface structure and optimized bond strengths between the NiSeTe surface and intermediate adsorbates.[22,48]

The long-term chronoamperometric stability of NiSeTe for 12 h (**Figure 7**a) showed excellent catalytic stability with no significant degradation under uninterrupted OER conditions at constant 1.51 V. Furthermore, the LSV polarization curves of NiSeTe before and after the chronoamperometry study were almost identical as illustrated by inset of Figure 7a.

This indicates the outstanding mass transfer property and mechanical robustness of the NiSeTe electrode. The chemical states and composition of the NiSeTe surface before and after stability showed that the catalyst is less susceptible to self-oxidation or corrosion, contrary to the belief that NiOOH formed on the catalyst surface during OER is the real active catalyst in nickel chalcogenide catalysts.[38,49] Surface Raman spectral analysis reveals no formation of extra Ni-oxide phases on the surface as shown in Figure 7b. Also, there is no change in the

relative intensity of the O $1s$ peak in the XPS spectrum before and after stability, suggesting no surface oxide layer formation (Figure S12, Supporting Information). Post-OER XPS analysis of NiSeTe indicates no increase in the intensity of the SeOx peak (inset of Figure 7d), consistent with the Raman results. The metallic nickel peak at 853.1 eV (Figure 7c) and the tiny Te satellite peaks at 573.0 and 583.4 eV originating from precursor-based surface impurities were absent after activity (Figure 7d). NiSeTe electrocatalysts indicated the least tendency toward oxidation compared to the other nickel chalcogenide catalysts, thereby preserving the structural coordination of NiSeTe in an alkaline medium. Similar observations have been made in NiSSe systems[37] and nickel chalcogenide systems.[25] Furthermore, the OER with NiSeTe may operate via a similar mechanism reported for other nickel chalcogenides, initiated by hydroxyl attachment on the catalytic site on the surface.[22,37] This will form hydroxylated nickel mixed anionic (hydroxy)-telluro-selenide (Ni(OH)SeTe) as possible intermediate species.

The chronoamperometric study of NiSe@NiTe at a constant applied potential of 1.52 V for 12 h suggests that there is no degradation in the catalytic activity of NiSe@NiTe. The polarization curves compared before and after chronoamperometry (Figure S8, Supporting Information) shows identical activity, suggesting excellent stability of the NiSe@NiTe composite under OER condition. The Raman spectra and XPS of NiSe@NiTe after chronoamperometry were analyzed. The Ni spectrum after chronoamperometry study shows additional peaks after deconvolution, corresponding to Ni $2p_{3/2}$ and Ni $2p_{1/2}$ of Ni^{3+} at 857.9 and 875.5 eV respectively (Figure S8, Supporting Information).
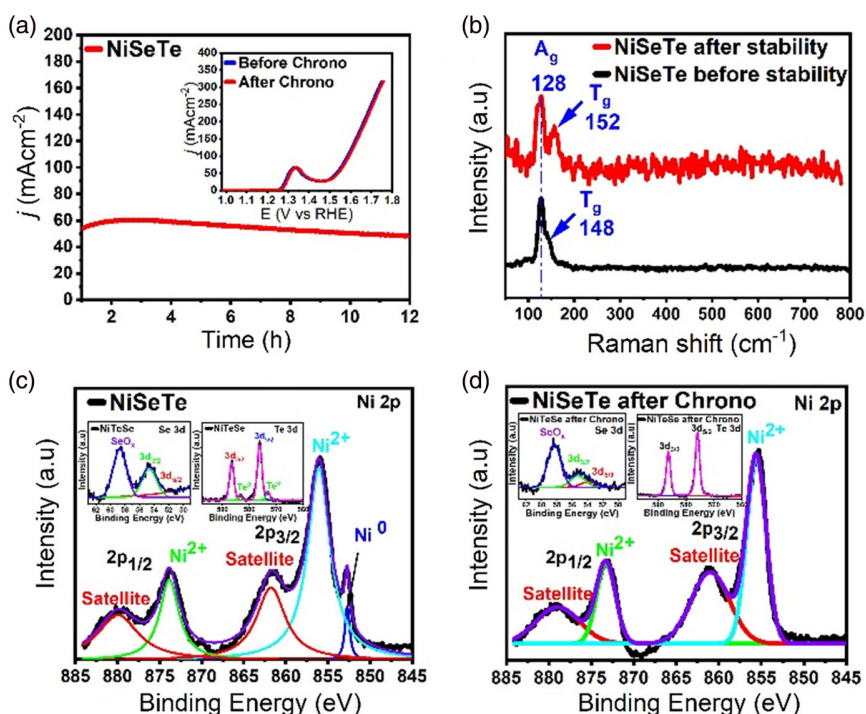

Figure 7. Chronopotentiometry curve of the NiSeTe recorded at 1.51 V for 12 h. a) The inset corresponds to the LSV of NiSeTe before and after chronoamperometry; b) Raman spectrum of NiSeTe before and after stability (chronoamperometry). The high-resolution XPS spectra of c) NiSeTe, Ni $2p$; d) NiSeTe after chronoamperometry, Ni $2p$. The left side insets correspond to Se $3d$ peaks, while the left side insets correspond to Te $3d$ peaks.

**ADVANCED
SCIENCE NEWS**

www.advancedsciencenews.com

Energy Technology
Generation, Conversion, Storage, Distribution

www.entechnol.de

This Ni oxidation is consistent with what was previously observed for NF/NiSe catalysts,[38] although it is very minimal in this composite catalyst, indicating that substrate and composition play a role in the oxidation process. Also, the peaks for Te at 576.3 and 586.9 eV corresponding to $3d_{5/2}$ and Te $3d_{3/2}$ become more visible, indicating increased porosity of the surface NiSe layer. Similar observations were made in previous reports.[41,50] However, the XPS spectra of Se before and after chronoamperometry study look very similar. The peak at around 58.9 eV for SeO_x increases slightly due to minimal oxidation on the surface of this catalyst (inset Figure S8 and S13, Supporting Information). Overall, there is no indication of drastic change in the surface composition of the NiSe@NiTe catalyst.

A similar observation was made for NiTe@NiSe at a constant applied potential of 1.58 V over 12 h. The polarization curve before and after chronoamperometry (Figure S13, Supporting Information) shows no significant change in activity. Raman spectroscopy and XPS before and after stability show that the identity of the catalyst was retained after chronoamperometry (Figure S9 and S14, Supporting Information). The XPS spectrum after chronoamperometry studies shows no additional peaks after deconvolution, implying no nickel oxide formation. Again, this suggests that the composite setup minimizes nickel oxidation from the NF substrate. The peaks for Te at 576.3 and 586.9 eV correspond to $3d_{5/2}$ and Te $3d_{3/2}$ remain at the same position after chronoamperometry, and no Se was detected before and after chronoamperometry, suggesting NiTe covers the bottom layer effectively. The excellent stability of NiTe@NiSe and NiSe@NiTe could be from the synergistic effect of the interaction of the two compositions in each composite. The chronoamperometry of NiSe shows high surface oxidation as indicated by the high relative intensity of SeO_x XPS peak after stability (Figure S15, Supporting Information). The Raman shows a shift in E_g peak, which supports this claim. While NiTe shows no significant changes in both Raman and XPS (Figure S15 and S16, Supporting Information), indicating that NiTe is more stable than NiSe under the tested reaction conditions.

3. DFT Studies

OER in an alkaline medium is a complex multistep process, initiated by a hydroxyl group ($–OH^-$) adsorption at the catalytic site which is considered the activation step.[51] Besides, it is well understood that the kinetics of the OER is estimated by the rate-determining step. This happens either during: 1) the first or second ^-OH attachment on the catalyst surface; or 2) the release of O_2. In both cases, the activation step is strongly influenced by the optimal surface coverage of the $–OH^-$ on the catalytic surface which lowers OER onset potential.[52] Understanding the catalyst activation step following $–OH$ adsorption on the surface-active site is crucial in providing detailed insights into the catalytic activities. The $–OH$ adsorption energy on the different catalyst surfaces as reported in this article was calculated through DFT, details of which have been provided in the supplementary material. The crystal structures of NiSe, NiTe, and NiSeTe were constructed from reported crystallographic data. Atomic positions of bulk NiSe, NiTe, and NiSeTe were relaxed, and their optimized geometries were used to construct slab models of NiSe, NiTe, and NiSeTe configurations. During the calculations, a relatively large vacuum space of 20 Å was set in the direction perpendicular to the xy-plane of the slab model (**Figure 8**). This is to avoid interaction with the periodic images of the lower layer.

NiSe belongs to the hexagonal crystal system with a space group of $P6_3/mmc$.[53] Similarly, NiTe also belongs to the hexagonal crystal system ($P6_3/mmc$).[54] On the contrary, NiSeTe crystallizes in a different structure, belonging to the trigonal crystal system.[31] The crystal structures of bulk NiSe, NiTe, and NiSeTe are shown in **Figure 9**a–c. The DFT-optimized lattice constant and bond lengths of NiSe, NiTe, and NiSeTe bulk structures are provided in **Table 2**.

The active Ni site in each configuration was selected and the system was relaxed to find the most stable binding location and corresponding energy. The $–OH^-$ ion was placed to the surface of the NiSe, NiTe, and NiSeTe slab structures in three different orientations: H-down, O-down, and OH-horizontal. Nine
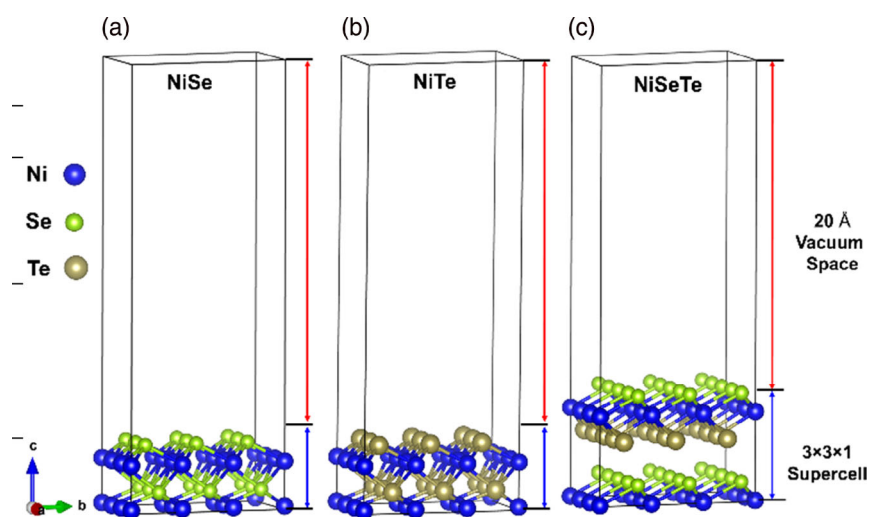

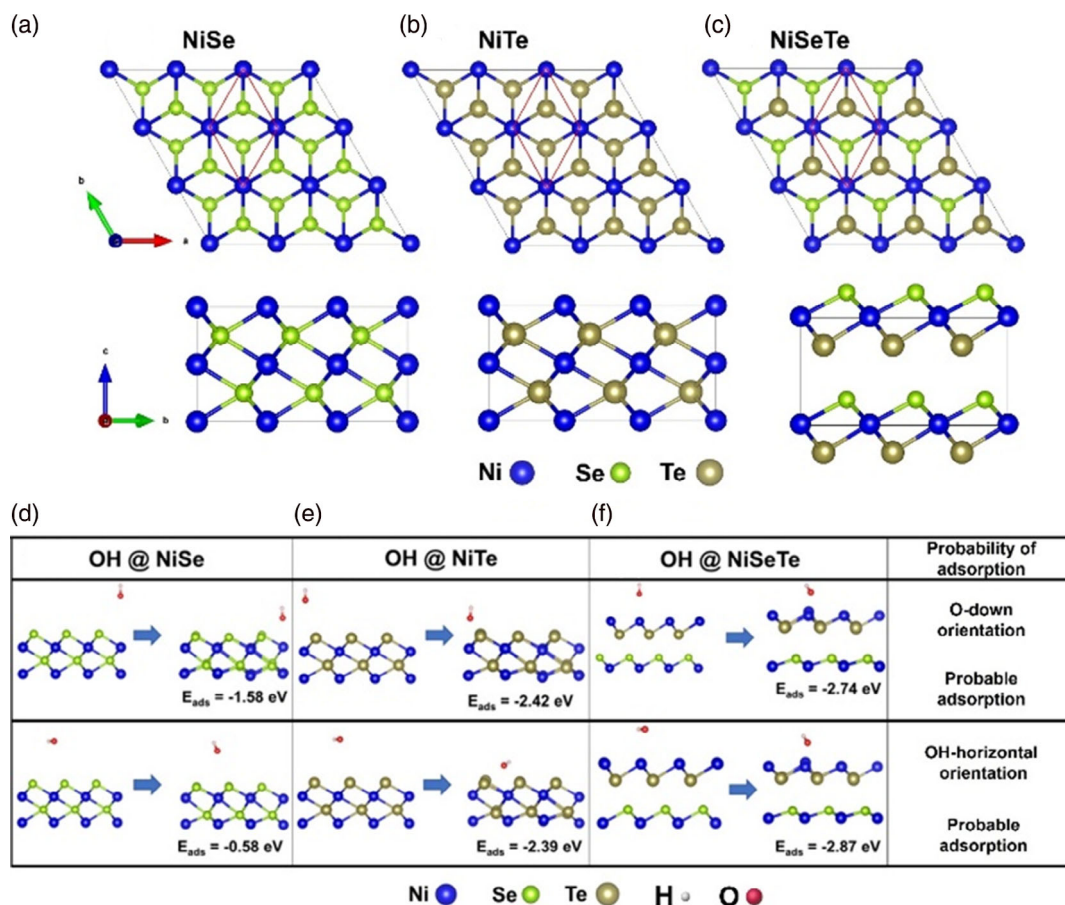**Figure 8.** Slab models of a) NiSe, b) NiTe, and c) NiSeTe supercells.

Figure 9. Crystal structures of 3 × 3 × 1 supercells of bulk a) hexagonal NiSe, b) hexagonal NiTe, and c) trigonal NiSeTe. In each configuration, Ni atoms are the active sites for OH adsorption and the unit cell are marked as a red rhombus. Original and relaxed structures of d) NiSe; e) NiTe; and f) NiSeTe, supercell slab models with an ‾OH ion adsorbed on the active Ni site.

Table 2. DFT optimized lattice constant and bond lengths of bulk NiSe, NiTe, and NiSeTe structures.

Structure	Crystal system	Space group	Lattice constant [Å]	Bond length [Å]				
				Ni–Se	Ni–Te	Se–Te [V][a]	Se–Se [V][a]	Te–Te [V][a]
NiSe	Hexagonal	$P6_3/mmc$	3.659	2.476	–	–	3.337	
NiTe	Hexagonal	$P6_3/mmc$	3.974	–	2.642	–	–	3.482
NiSeTe	Trigonal	$P\bar{3}m1$	3.757	2.458	2.562	3.332	5.049	5.049

[a]The (V) in bond length denotes the vertical distance between two adjacent atoms.

different DFT calculations were carried out to cover all possible configurations to compute the adsorption energy of –OH on the Ni-series surface. The H-down orientation gives the least favorable adsorption (Figure S17, Supporting Information) because –OH adsorptions are expected to be directed toward the active Ni site through the more electronegative oxygen atom. Hence, the more probable –OH adsorption approaches are O-down and –OH-horizontal orientations, as shown in Figure 9d–f. Previous studies reported that stable –OH adsorptions (energetically favorable) are facilitated by decrease (more negative) in adsorption energy.[48] A comparative analysis of the –OH

adsorption energies on the different catalyst sites is shown in **Figure 10**a. The O-down orientation on NiTe and NiSeTe shows superior binding energy of −2.42 and −2.74 eV, respectively. Similarly, the –OH-horizontal orientation shows stable binding energy of −2.39 and −2.87 eV on NiTe and NiSeTe, respectively (Figure 10a). This shows that the more probable –OH adsorption orientations display consistent and favorable –OH adsorption energies.[48] However, NiSe showed wider adsorption energy difference with change in –OH orientation. This indicates that effects of anion electronegativity in the nearest neighbor coordination and molecular orientation could affect –OH adsorption
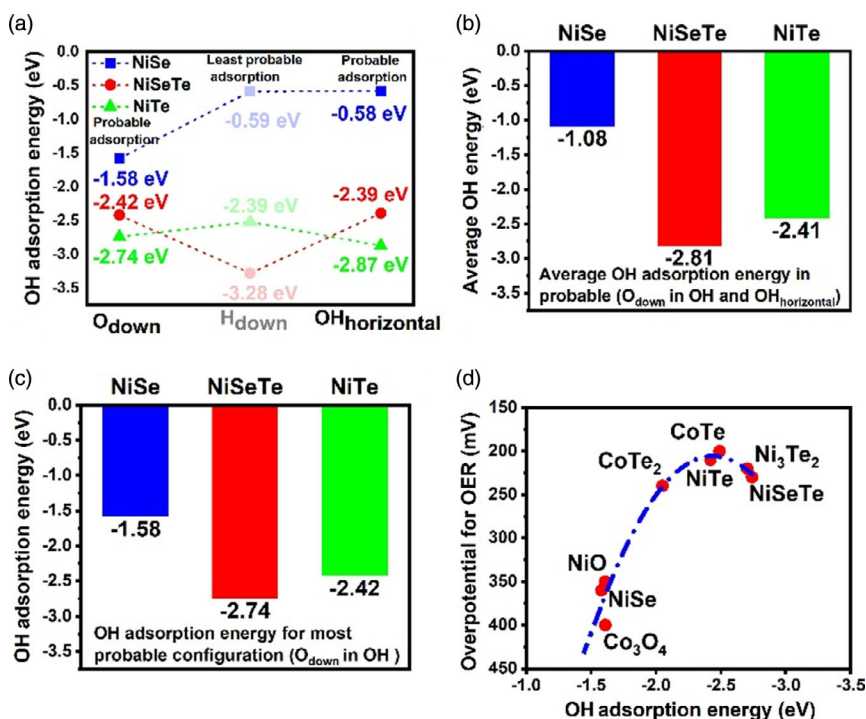
ADVANCED
SCIENCE NEWS
www.advancedsciencenews.com

Energy Technology
Generation, Conversion, Storage, Distribution
www.entechnol.de

Figure 10. a) The adsorption energy of $^-$OH at different orientations, when placed on top of the slab model of NiSe, NiTe, and NiSeTe; b) average adsorption energy of $^-$OH for the most probable orientations when placed on top of the slab model of NiSe, NiTe, and NiSeTe; c) calculated adsorption energy of $^-$OH$^-$ ions on NiSe, NiSeTe, and NiTe for O-down in $^-$OH (most probable adsorption configuration). The more negative value indicates the lower adsorption energy; d) graph of overpotential as a function of $^-$OH adsorption energy for various OER catalysts revealing a dependence, similar to the rising part of a volcano plot.

energy of catalysts. The –OH adsorption energy analysis indicates that an energetically favorable –OH adsorption on the surface of Ni-site may lead to optimal surface coverage and activation resulting in faster onset of OER catalytic activity. This is a critical precondition for superior OER performance. Hence, the average –OH adsorption energy for the more probable orientations (O-down and –OH-horizontal) was computed (Figure 10b), and it was observed that NiTe ($E_{ave\ ads}$: -2.41 eV) has higher adsorption energy than NiSeTe ($E_{ave\ ads}$: -2.81 eV). These results indicate that the adsorption of –OH on NiSeTe is more spontaneous and therefore energetically more favorable than that of NiTe and NiSe. This suggests that –OH adsorption is affected by changes in crystal structure and anion composition.

Conventionally, adsorptions with O-down in –OH orientation are employed for benchmark comparison because they are considered more likely. Under this orientation, NiSeTe shows very low adsorption energy, making it highly favorable (Figure 10c). This is consistent with the high activity of NiSeTe toward OER reaction. However, to adequately assess the significance of the $^-$OH adsorption on observed OER performance, we plotted OER overpotential as a function of –OH adsorption energy to create a volcano plot. This included few known catalysts (NiO, Ni_3Te_2, Co_3O_4, CoTe, and $CoTe_2$),[20] along with NiSe, NiTe, and NiSeTe as shown in Figure 10d.

It should be noted that the –OH adsorption energies for all these catalyst surfaces (NiO, Ni_3Te_2, Co_3O_4, CoTe, $CoTe_2$, NiSe, NiTe and NiSeTe) were estimated following similar

protocol and treated under similar conditions. It was observed that as the –OH adsorption energy increases, the overpotential also decreases down to a minimum overpotential and then starts to increase. This resembles the rising part of a volcano or Sabatier plot,[20,51,55,56] indicating that there is an optimum -OH adsorption energy for best OER activity, which is around (-2.5 eV) in this work. Such relationship between OH adsorption energy and OER overpotential can play a critical role in catalyst surface design by providing a simple descriptor for benchmarking catalyst efficiencies, which significantly simplifies catalytic surfaces comparison by reducing computational time to.[55,56]

Furthermore, the adsorption distance of –OH from the surface of NiSe, NiTe, and NiSeTe was estimated, and it was observed that they all possess stable adsorption distances, as shown in **Table 3**. The computed adsorption distance of –OH from the Ni site of NiSe, NiTe, and NiSeTe is 2.789, 3.931, and 1.821 Å, respectively. Bader charge analysis was performed to study the charge transfer between the –OH ion and Ni-series.

The charge transfer is primarily ascribed to the difference in the electronegativity of the anions, which coupled with chemical bonding is theoretically associated with the adsorption energy. In general, strong adsorption energy denotes a strong chemical bond, whereas low adsorption energy indicates a weak chemical and/or van der Waals bond.[57] During the adsorption of –OH ion on the surface Ni-site along the series, the charge is transferred from the –OH ion to the surface and the computed charges

Table 3. The bond length of −OH-adsorbed NiSe, NiTe, and NiSeTe configurations as well as the shortest distance between -OH and the Ni-series.

System[a]	Bond length									Charge e	Style (Ni site)
	Ni–Ni	Ni–Se	Se–Se	Ni–Te	Te–Te	Se–O	Te–O	Ni–O	Ni–H		
NiSe + OH	3.496	2.385	3.608	–	–	2.702		2.789	–	−0.280	Acceptor
NiTe + OH	3.890	–	–	2.585	3.911		2.021	3.931	–	−0.233	Acceptor
NiSeTe + OH	3.752	2.272	3.774	2.431	3.743	–	–	1.821	2.398	−0.307	Acceptor

[a]Computed Bader charge of −OH-adsorbed Ni series is also provided. The OH molecule acts as a charge acceptor with considerable exchange of charges with the Ni-series and is reflected in the adsorption energy.

are −0.280, −0.233, and −0.307 e for NiSe, NiTe, and NiSeTe, respectively. The charge density of isolated NiSe, NiTe, and NiSeTe structures and −OH ion is computed under the same adsorbed configuration. In Figure S17, Supporting Information, we show the isosurface of the electronic CDD during the interaction of the −OH ion and the surface of the Ni series. The electron density accumulation and depletion can be correlated with the transfer of charges from the −OH ion to the surface.

The electronic properties of the slab models of the Ni-series and the computed band structure along with the high-symmetry points Γ–M–K–Γ–A–L–H–A are shown in Figure S18, Supporting Information. We noticed that all the studied configurations show metallic characteristics, as there is no gap between the valence and conduction bands and a finite density of states (DOS) is present at the Fermi level. To obtain a deeper understanding of the electronic properties of bulk NiSe, NiTe, and NiSeTe structures, we analyzed the total and projected density of states (TDOS and PDOS) which are shown in Figure S19 and S20, Supporting Information, respectively. The electronic property analysis revealed that the DOS at and around the Fermi level of all the studied configurations is dominated by the contribution of Ni atoms. The metallicity in NiSe, NiTe, and NiSeTe structures is mainly due to the partially occupied bands in the conduction band. The PDOS of NiSe, NiTe, and NiSeTe in Figure S20, Supporting Information shows that valence band maximum (VBM) and conduction band minimum (CBM) mainly dominate from the d-orbital of Ni and p-orbital of Se/Te, respectively. In VBM, orbital mixing between Ni (d_z^2), and Ni (d_{xz}, d_x^2–d_y^2) orbitals was observed in the range of 0–2.0 eV, while the p_x orbital of the Se/Te atom was larger compared to d-orbital of Ni. Although the p-orbitals of Se/Te are dominant around the Fermi level, the metallicity in NiSe, NiTe, and NiSeTe is mainly due to the d-orbitals.

Furthermore, to understand the theoretical insights into the electronic properties of −OH-adsorbed Ni-series, we analyzed the band structure, total, and projected DOS. We observed significant differences in the band structure of −OH-adsorbed NiSe, NiTe, and NiSeTe structures compared to the bulk models. With the presence of −OH ion, the conduction bands are shifted more toward the Fermi level, and an enhanced conductivity is observed. This increase in conductivity mainly arises from the shifting of valence bands up, as shown in Figure S21, Supporting Information. The total DOS analysis reveals the metallic nature of −OH-adsorbed Ni-series shown in Figure S22, Supporting Information, which shows features

similar to the slab structure of the Ni-series. The metallicity in the −OH-adsorbed surfaces was observed to mainly come from the Ni atoms. Similarly, for −OH-adsorbed NiSe and NiTe, the PDOS analysis reveals that the VBM and CBM mainly dominate from the d-orbital of Ni and p-orbital of Se/Te. In VBM, orbital mixing between Ni (d_z^2) and Ni (d_{xz}, d_x^2–d_y^2) orbitals was observed in the range of 0– −2.0 eV, while the p_x orbital of the Se/Te atom was larger than the d-orbital of Ni, as shown in Figure S23, Supporting Information. Significant contributions from the p_x and p_y orbitals of O atoms around the Fermi level were also observed for −OH-adsorbed NiSe. However, it is interesting to note that although the −OH-adsorbed NiTe is showing metallicity at and around the Fermi level, the contributions from the O atoms in the −OH is insignificant compared to O atoms in the −OH of NiTe. Furthermore, the PDOS of −OH-adsorbed NiSeTe was analyzed and the presence of DOS at and around the Fermi level was observed. This comes from the contribution of the d_{xz}, d_x^2–d_y^2, and d_z^2 orbitals of Ni atoms, and p_x and p_z orbitals of Se and Te atoms, as shown in Figure S24, Supporting Information. Also, it was observed that the contribution from the p_z and p_y orbitals of O atoms in the −OH adsorbed NiSeTe is also significant and is essentially different from the −OH adsorbed NiSe and NiTe. Nonetheless, as the catalytic activity of the catalyst is strongly influenced by the electronic states, all the −OH adsorbed Ni-series show superior electrical conductivity and are suitable for electrochemical water-splitting applications.

4. Conclusion

We presented in situ hydrothermal growth of NiSeTe, NiSe, NiTe, (NiSe@NiTe), and (NiTe@NiSe) as efficient, high-performance, and durable OER electrocatalysts. The NiSe@NiTe and NiTe@NiSe were found to be phase-layered systems, each containing mixture NiSe and NiTe phases. Nickel (telluro)-selenide (NiSeTe) was found to be a single pure phase as indicated by XRD and EDX and allow excellent OER catalysis with ultralow overpotentials of 300 mV at 50 mA cm^{-2}, small Tafel slope of 98 mV dec^{-1}, high TOF (0.047 s^{-1}), and mass activity (90.3 Ag^{-1}), superior to numerous nonprecious OER catalysts in the literature. This highlights the effect of changing anion coordination geometry, crystal lattice structure, and electronic density around the metal center in OER performance. The stability and durability of the catalysts suggest that this facile fabrication approach minimizes catalyst surface oxidation. This can also be associated with the interfacial synergistic effect between NiSe

and NiTe in the layered samples. This work unlocks exciting new avenues to explore transition-metal mixed anionic chalcogenides to understand structure−property−performance relationships in catalysts and their electrochemical applications. DFT calculations of −OH adsorption energy, electronic, and charge transfer properties provide insights into the mechanism of improved OER catalytic activity in the NiSeTe.

Supporting Information

Supporting Information is available from the Wiley Online Library or from the author.

Conflict of Interest

The authors declare no conflict of interest.

Data Availability Statement

The data that support the findings of this study are available from the corresponding author upon reasonable request.

[1] J. A. Turner, *Science (1979)* **2004**, *305*, 972.
[2] K. Zeng, D. Zhang, *Prog. Energy Combust. Sci.* **2010**, *36*, 307.
[3] M. G. Walter, E. L. Warren, J. R. McKone, S. W. Boettcher, Q. Mi, E. A. Santori, N. S. Lewis, *Chem. Rev.* **2010**, *110*, 6446.
[4] D. M. F. Santos, C. A. C. Sequeira, D. Macciò, A. Saccone, J. L. Figueiredo, *Int. J. Hydrogen Energy* **2013**, *38*, 3137.
[5] Z. Wang, J. Yang, J. Gan, W. Chen, F. Zhou, X. Zhou, Z. Yu, J. Zhu, X. Duan, Y. Wu, *J. Mater. Chem. A Mater.* **2020**, *8*, 10755.
[6] Y. Lee, J. Suntivich, K. J. May, E. E. Perry, Y. Shao-Horn, *J. Phys. Chem. Lett.* **2012**, *3*, 399.
[7] J. K. Nørskov, T. Bligaard, J. Rossmeisl, C. H. Christensen, *Nat. Chem.* **2009**, *1*, 37.
[8] Y. Meng, M. Wang, Z. Zhu, T. Jiang, Z. Liu, N. Chen, C. Shen, Q. Peng, W. Chen, *ACS Appl. Energy Mater.* **2021**, *4*, 12927.
[9] P. W. Menezes, C. Panda, S. Loos, F. Bunschei-Bruns, C. Walter, M. Schwarze, X. Deng, H. Dau, M. Driess, *Energy Environ. Sci.* **2018**, *11*, 1287.
[10] X. Wang, W. Li, D. Xiong, L. Liu, *J. Mater. Chem. A Mater.* **2016**, *4*, 5639.
[11] X. Y. Wang, X. P. Han, Y. He, W. bin Hu, Y. da Deng, *Int. J. Electrochem. Sci.* **2020**, *15*, 3563.
[12] A. T. Swesi, J. Masud, M. Nath, *Energy Environ. Sci.* **2016**, *9*, 1771.
[13] Y. Li, C. Zhao, *Adv. Mater. Lett.* **2017**, *8*, 916.
[14] Z. Wang, L. Zhang, *Electrochem. Commun.* **2018**, *88*, 29.
[15] Y. Rao, Y. Wang, H. Ning, P. Li, M. Wu, *ACS Appl. Mater. Interfaces* **2016**, *8*, 33601.
[16] I. M. Abdullahi, J. Masud, I. Polydoros-Chrisovalantis, E. Ferentinos, P. Kyritsis, M. Nath, *Molecules* **2021**, *26*, 945.
[17] J. Masud, P. C. Ioannou, N. Levesanos, P. Kyritsis, M. Nath, *ChemSusChem* **2016**, *9*, 3128.
[18] E. J. Popczun, J. R. McKone, C. G. Read, A. J. Biacchi, A. M. Wiltrout, N. S. Lewis, R. E. Schaak, *J. Am. Chem. Soc.* **2013**, *135*, 9267.
[19] J. Tian, Q. Liu, A. M. Asiri, X. Sun, *J. Am. Chem. Soc.* **2014**, *136*, 7587.
[20] M. Nath, U. de Silva, H. Singh, M. Perkins, W. P. R. Liyanage, S. Umapathi, S. Chakravarty, J. Masud, *ACS Appl. Energy Mater.* **2021**, *4*, 8158.
[21] L. Liao, S. Wang, J. Xiao, X. Bian, Y. Zhang, M. D. Scanlon, X. Hu, Y. Tang, B. Liu, H. H. Girault, *Energy Environ. Sci.* **2014**, *7*, 387.
[22] X. Cao, J. E. Medvedeva, M. Nath, *ACS Appl. Energy Mater.* **2020**, *3*, 3092.
[23] A. T. Swesi, J. Masud, W. P. R. Liyanage, S. Umapathi, E. Bohannan, J. Medvedeva, M. Nath, *Sci. Rep.* **2017**, *7*, 2401.
[24] U. de Silva, J. Masud, N. Zhang, Y. Hong, W. P. R. Liyanage, M. Asle Zaeem, M. Nath, *J. Mater. Chem. A Mater.* **2018**, *6*, 7608.
[25] U. de Silva, J. See, W. P. R. Liyanage, J. Masud, J. Wu, W. Yang, W. T. Chen, D. Prendergast, M. Nath, *Energy Fuels* **2021**, *35*, 4387.
[26] F. A. Rasmussen, K. S. Thygesen, *J. Phys. Chem. C* **2015**, *119*, 13169.
[27] Y. Liu, P. Vijayakumar, Q. Liu, T. Sakthivel, F. Chen, Z. Dai, *Nano-Micro Lett.* **2022**, *14*, 43.
[28] S. He, H. Lin, R. Sun, Z. Wang, *2D Mater.* **2020**, *7*, 041001.
[29] C. de las Heras, F. Agullo-Rueda, *J. Phys. Condens. Matter* **2000**, *12*, 5317.
[30] H. Zhou, Y. Wang, R. He, F. Yu, J. Sun, F. Wang, Y. Lan, Z. Ren, S. Chen, *Nano Energy* **2016**, *20*, 29.
[31] F. Hulliger, *J. Phys. Chem. Solids* **1965**, *26*, 639.
[32] I. M. Abdullahi, M. Langenderfer, O. Shenderova, N. Nunn, M. D. Torelli, C. E. Johnson, V. N. Mochalin, *Carbon N Y* **2020**, *164*, 442.
[33] J. I. Langford, J. C. Wilson, *J. Appl. Cryst.* **1978**, *11*, 102.
[34] Z. Xue, X. Li, Q. Liu, M. Cai, K. Liu, M. Liu, Z. Ke, X. Liu, G. Li, *Adv. Mater.* **2019**, *31*, 1900430.
[35] Q. Peng, Q. He, Y. Hu, T. T. Isimjan, R. Hou, X. Yang, *J. Energy Chem.* **2022**, *65*, 574.
[36] Y. Li, B. Chen, H. Zhang, J. Gao, H. Sun, A. Habibi-Yangjeh, C. Wang, *ChemElectroChem* **2021**, *8*, 3643.
[37] B. R. Wygant, A. H. Poterek, J. N. Burrow, C. B. Mullins, *ACS Appl. Mater Interfaces* **2020**, *12*, 20366.
[38] C. Tang, N. Cheng, Z. Pu, W. Xing, X. Sun, *Angew. Chem. Int. Ed.* **2015**, *54*, 9351.
[39] C. Liu, K. Wang, X. Zheng, X. Liu, Q. Liang, Z. Chen, *Carbon* **2018**, *139*, 1.
[40] S. Chen, J. L. Mi, P. Zhang, Y. H. Feng, Y. C. Yong, W. D. Shi, *J. Phys. Chem. C* **2018**, *122*, 26096.
[41] S. Shit, S. Chhetri, W. Jang, N. C. Murmu, H. Koo, P. Samanta, T. Kuila, *ACS Appl. Mater. Interfaces* **2018**, *10*, 27712.

**ADVANCED
SCIENCE NEWS**

www.advancedsciencenews.com

Energy Technology
Generation, Conversion, Storage, Distribution

www.entechnol.de

[42] L. Trotochaud, S. L. Young, J. K. Ranney, S. W. Boettcher, *J. Am. Chem. Soc.* **2014**, *136*, 6744.

[43] A. S. Batchellor, S. W. Boettcher, *ACS Catal.* **2015**, *5*, 6680.

[44] V. Freger, *Electrochem. Commun.* **2005**, *7*, 957.

[45] X. Zhang, Y. Ding, G. Wu, X. Du, *Int. J. Hydrogen Energy* **2020**, *45*, 30611.

[46] M. Li, L. Feng, *Jiegou Huaxue* **2022**, *41*, 2201019.

[47] G. A. Gebreslase, M. V. Martínez-Huerta, M. J. Lázaro, *J. Energy Chem.* **2022**, *67*, 101.

[48] X. Cao, Y. Hong, N. Zhang, Q. Chen, J. Masud, M. A. Zaeem, M. Nath, *ACS Catal.* **2018**, *8*, 8273.

[49] M. W. Louie, A. T. Bell, *J. Am. Chem. Soc.* **2013**, *135*, 12329.

[50] X. Ma, J. Yang, X. Xu, H. Yang, C. Peng, *RSC Adv.* **2021**, *11*, 34432.

[51] N. T. Suen, S. F. Hung, Q. Quan, N. Zhang, Y. J. Xu, H. M. Chen, *Chem. Soc. Rev.* **2017**, *46*, 337.

[52] T. Shinagawa, A. Garcia-Esparza, K. Takanabe, *Sci. Rep.* **2015**, *5*, 13801.

[53] F. Grqlnvold, E. Jacobsen, *Acta Chem. Scand.* **1956**, *10*, 1440.

[54] L. Norén, V. Ting, R. L. Withers, G. van Tendeloo, *J. Solid State Chem.* **2001**, *161*, 266.

[55] W. T. Hong, M. Risch, K. A. Stoerzinger, A. Grimaud, J. Suntivich, Y. Shao-Horn, *Energy Environ. Sci.* **2015**, *8*, 1404.

[56] M. J. Craig, G. Coulter, E. Dolan, J. Soriano-López, E. Mates-Torres, W. Schmitt, M. García-Melchor, *Nat. Commun.* **2019**, *10*, 4993.

[57] S. Thomas, M. Asle Zaeem, *Appl. Surf. Sci.* **2021**, *563*, 150232.